The Henryk Niewodniczański
INSTITUTE OF NUCLEAR PHYSICS
Polish Academy of Sciences
ul. Radzikowskiego, 31-342 Kraków, Poland

www.ifj.edu.pl/publ/reports/2009/

Kraków, March 2009

Report No. 2025/AP

Multipurpose X-ray microprobe in the IFJ PAN
Technical description

J. Bielecki, S. Bożek[1], A. Banaś[2], J. Baszak[3], H. Doruch, R. Hajduk, J. Kowalska, T. Pieprzyca, Z.Szklarz, J. Lekki, Z. Stachura, W.M. Kwiatek

[1] *IFJ PAN and the Jagiellonian University Medical College, Cracow, Poland*
[2] *on leave to the Singapore Synchrotron Light Source, National University of Singapore*
[3] *jbaszak@hamamatsu.de*

Multipurpose X-ray microprobe in the IFJ PAN – Technical description

J. Bielecki, S. Bożek[1], A. Banaś[2], J. Baszak[3], H. Doruch, R. Hajduk, J. Kowalska, T. Pieprzyca, Z.Szklarz, J. Lekki, Z. Stachura, W.M. Kwiatek

The Henryk Niewodniczański Institute of Nuclear Physics, Polish Academy of Sciences (IFJ PAN), Cracow, Poland

[1]IFJ PAN and the Jagiellonian University Medical College (JU MC), Cracow, Poland

[2]on leave to the Singapore Synchrotron Light Source, National University of Singapore (SSLS)

[3]jbaszak@hamamatsu.de

1. INTRODUCTION

The nuclear microprobe at the IFJ PAN in Cracow has found numerous applications in different fields of research, mostly in biophysics, medical sciences, geology, and materials research. In order to extend the research possibilities, a new X-ray microprobe has been constructed. This new microprobe consists of three experimental lines dedicated to: i) computed microtomography (CMT), ii) X-ray irradiation of biological specimens and iii) elemental analysis of samples by micro-X-ray fluorescence (μXRF) and total reflection X-ray fluorescence (TXRF) methods. In the future also other applications of the microprobe are foreseen, including the small angle X–ray scattering (SAXS) and the micro-crystallography measurements. The common element applied in all lines is a source of X-ray radiation – an open type, microfocusing X-ray tube Hamamatsu L9191 (Fig. 1), while other elements of experimental stands depend on the application of the radiation beam. Elements of the experimental lines are mounted on an anti-vibrational optical table with a breadboard produced by the Standa Co. (Lithuania) [1].

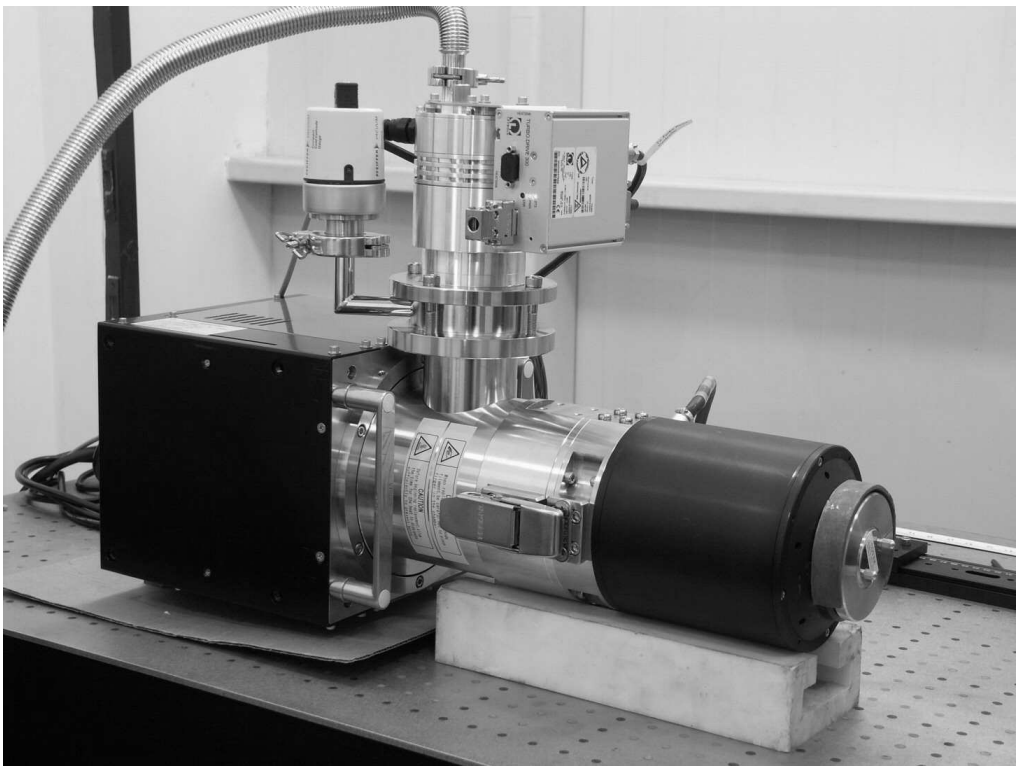

Fig. 1. Microfocusing X-ray tube Hamamatsu L9191

In order to protect experimentalists from the radiation, the tube and experimental lines are located inside a lead box with 3 mm thick lead walls covered with Cu + Al plates. The front wall of the box is a

movable window made of the 10 mm thick lead glass (Fig. 2). The present status of the microprobe (20 Jan. 2009) is as follows:

- CMT stand – ready to use, first routine experiments started
- stand for X-ray irradiations – in testing phase
- stand for μXRF and TXRF – components of the stand are completed, testing phase will start in summer 2009
- other experimental methods will be implemented in 2010.

Fig. 2. Optical table and radiation shielding of the X-ray microprobe

2. COMPUTED MICROTOMOGRAPHY (CMT) FACILITY

2.1. Radiation source and other components of the CMT stand

Figure 1 presents a schematic diagram of the experimental line dedicated to CMT experiments. The line consists of the X-ray tube as a source of radiation, an X-ray sensitive CCD camera, and a precise goniometer. The source-to-detector distance, usually set as 500 mm, can be extended to about 1 m while source-to-sample distance can be changed from below 1 mm to almost the source-to-detector distance ensuring a wide range of magnification tuning, from almost 1x to over 1500x. The cone beam geometry entails that projections have to be acquired with equiangular separation over 360°.

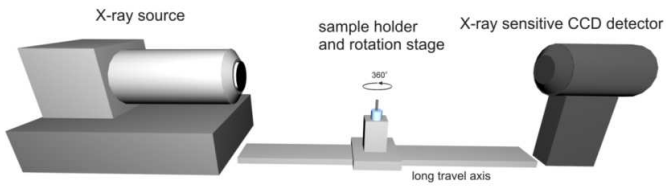

Fig. 3. Experimental line for the CMT experiments

A use of the microprobe is not restricted to one type of experiments, so it should be as universal as reasonably possible, delivering both hard and soft X-ray beam. Microscopic specificity of measurements requires that the radiation is emitted from a point-like source. In microtomography experiments this radiating spot can be located within the X-ray tube and the beam does not require any re-focusing outside the tube. After a search for the best suitable X-ray source, the Hamamatsu L9191 open type tube [2] was chosen (Fig. 1). This model has the extremely small X-ray emitting spot size, a wide range of accelerating voltage, and supports easily exchangeable anodes. Four different anodes ("targets") made of Titanium, Molybdenum, Silver, and Tungsten evaporated on a beryllium window are provided in order to tune the X-ray energy, which is adjusted to the specimen's density.

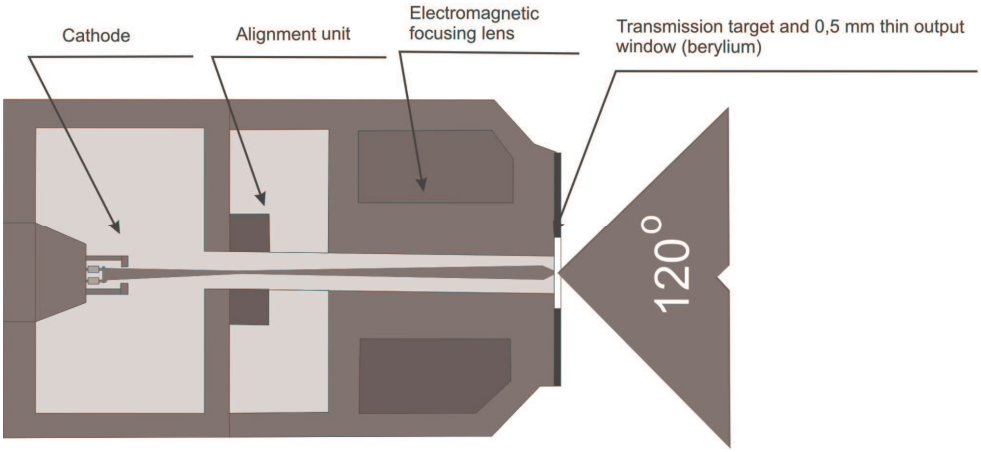

Fig. 4. Schematic diagram of the X-ray tube with the microfocusing system used for the CMT experiments

Acceleration voltage can be changed in the 20 - 160 kV range, whereas the tube current may be set up to 200 µA. Radiation is emitted from a small spot (less than 2 µm in diameter) into a cone (120 degrees opening angle) through 0.5 mm thick beryllium plate, being simultaneously a substrate for the target and the output window of the tube (Fig. 4). When the tube is working, the intense electron beam is sputtering the target material and after several weeks of work the beryllium window must be rotated, to allow for a use of the new, undamaged target area.

Fig. 5. Goniometer used in the CMT experiments

Positioning and rotating of a sample is accomplished with the use of six inertial piezoelectric motors produced by the Attocube Systems AG (Germany) [3]. Three of them are used to move the sample in the x-y-z directions. Another two motors enable tilting the rotation axis and the last one serves as a precise rotator. The actuators are stacked vertically and form a precise goniometer (Fig. 5). Maximum load for these devices is 100 grams. The accuracy of translation for linear motors reaches half micrometer, whereas angular precision for rotator is about 0.1". Three main motors are equipped with resistive readout encoders what enables the "on-line" measuring of the specimen position.

Image acquisition is accomplished with Photonic Science X-ray sensitive CCD camera (Fig.6) [4]. The sensor is composed of 4008 x 2670 pixels, readout at 10 MHz frequency, followed by digitization of the CCD signal to 12-bit accuracy (4096 grey levels). Each pixel has size of 14.7 µm in diameter. The CCD sensor is optically bonded to a tapered fibre-optic. The fibre ending has been covered with the X-ray scintillator (Gadolinium Oxysulphide doped with terbium, approximately 10 mg/cm2). The thickness of the scintillator is optimized to register X-rays of energies in a range of 5 to 35 keV. The image readout is carried out by means of a commercial frame grabber card installed in a personal computer. In

order to check linearity of the detector used for image acquisition in CMT experiments, the detector response as a function of tube current has been determined. The output signal was measured in the flat field mode by increasing the intensity of the X-ray beam up to the maximum signal amplitude value measurable by the CCD, with avoiding saturation. The X-ray tube was equipped with Ti target and set at 70 kV, varying its current from 1 to 10 µA. Source-to-detector distance was set to 410 mm. The output signal was first averaged over 5 frames and then averaged over a region-of-interest of about 4000x2500 pixels to minimize the effects of non-uniformity in the illumination. Fig. 7 shows the resulting response curve. The response signal is highly linear in a wide range of the absorbed dose of X-rays.

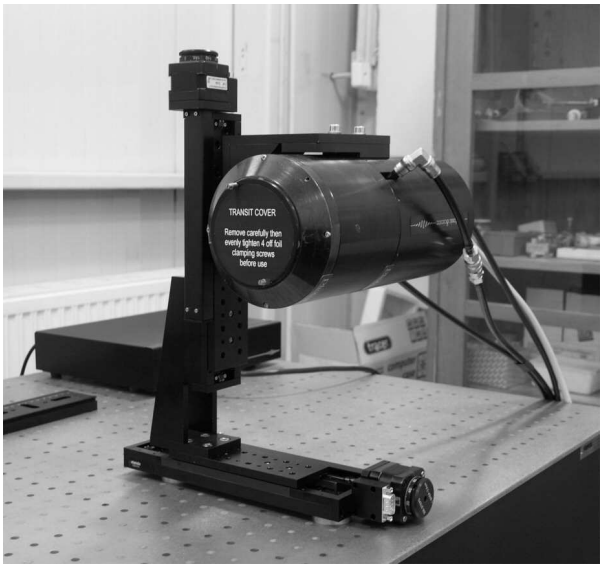

Fig. 6. X-ray sensitive CCD camera, Photonic Science VHR-70

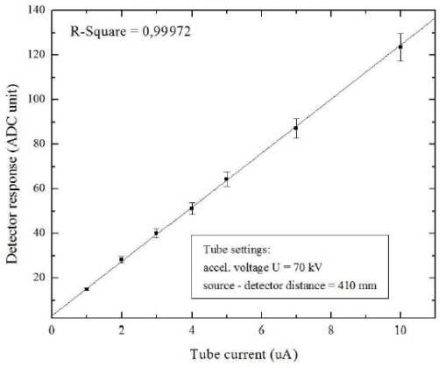

Fig. 7. The CCD detector response (ADC units) versus *X-ray tube current.*

2.2. Electronics and software associated with the CMT experiments

For image acquisition and experiment control a solution based on two PCs has been chosen. The first computer is dedicated to control the conditions of the experiment (monitoring and setting the x-ray tube parameters and readout and setting the sample position), while the second PC is used for data acquisition and analysis as well as for image reconstruction. Communication between the two PCs is accomplished with a use of TCP/IP protocol. Hardware modules used in the CMT experiment are functionally divided into three groups (Fig. 8). The first one, responsible for X radiation generation, consists of the X-ray tube, its controller, and the interlock system assuring the radiation

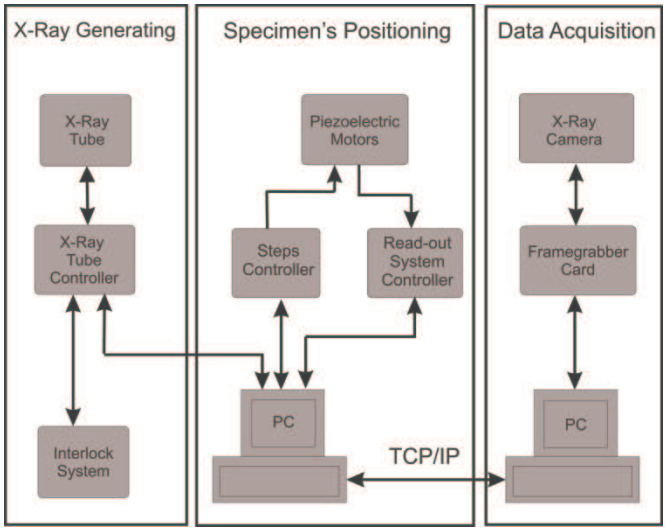

Fig 8. Electronics associated with CMT experiments.

safety. The X-ray tube controller is remotely controlled by a PC via the RS232 port. The two other PC serial ports are connected to units controlling positioning and movement of the measured specimen. The goniometer, composed of six inertial piezoelectric motors, is controlled by a steps controller connected to the PC. Actual position of the sample is registered in the computer through the read-out system controller, connected to the resistive encoders incorporated into piezoelectric motors. The last group of modules forms the data acquisition track. These are the X-ray sensitive CCD camera and a frame grabber card installed in a slot of the second PC.

Software system used in the CMT measurements is based on a few complementary computer programs – a home developed code as well as few commercial packages. Experiment is controlled by a home-made program written in C# which is linked with the Image Pro Plus package [5]. Projections, flat fields and dark images are stored in the TIFF format on the PC hard disks. These files are the input data for the reconstruction package. The Octopus package based on filtered back projection algorithm [6] is used for slices reconstruction. Reconstruction time of tomography image from a data set consisting of 500 projections each of 512x512 pixels, reconstructed in the cone beam geometry using the normal quality setting takes about 30 minutes at the PC computer with AMD Athlon X2 Dual Core 64 bit CPU and 2GB RAM memory. The 3D visualization and analysis is accomplished with the Avizo package [7]. Fig. 9 shows a diagram of the data flow in CT experiments.

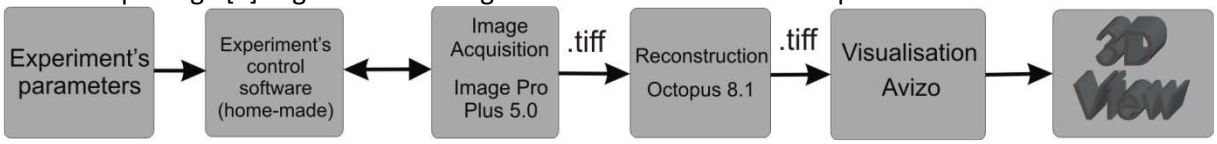

Fig. 9. Scheme of software system used in CMT measurement

2.3. Tests of the CMT facility

In order to evaluate the spatial resolution of the system a test with microfabricated pattern has been carried out. The pattern, produced nanolithographically by Xradia Ltd., is a circle composed of wedges 16 µm wide at the outer part of the circle and narrowing down to 0.5 µm for smaller radii [9]. Fig. 10 presents image of the pattern obtained with use of the X-ray microprobe.

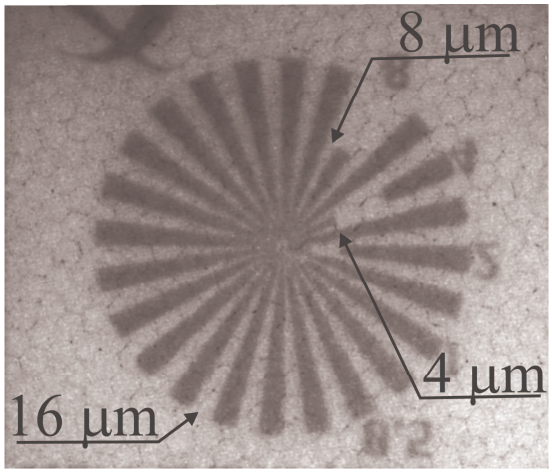

Fig. 10. X-ray image of the microfabricated pattern. The outside cogs have the size of 16 µm, cogs on the middle circumference have the size of 8 µm, and are narrowing down to 0.5 µm for the smallest radii.

The resolution can be estimated by observation of the smallest details of the pattern tile what can be optically resolved in the X-ray image. The exact numerical value of the resolution is evaluated by deconvolution process from a projection of the pattern X-ray image. A consequence of finite size of the radiation source is a smearing out of the sharp edges of the wedges image of the tile, and intensity of the projection image is a convolution of the wedge shape (a step function) and a size of the emission spot of X radiation. It is assumed that the X-ray intensity distribution within the spot is represented by a 2-dimensional Gaussian. An example of the deconvolution process is shown in Fig. 11. Statistical errors in the digitized X-ray projection images are much smaller than systematic errors caused by differences of sensitivity for

different pixels of the CCD camera or by instability of the electron beam current in the tube. Therefore, the resolution values of the tube presented in this paper are the average values of a series of measurements.

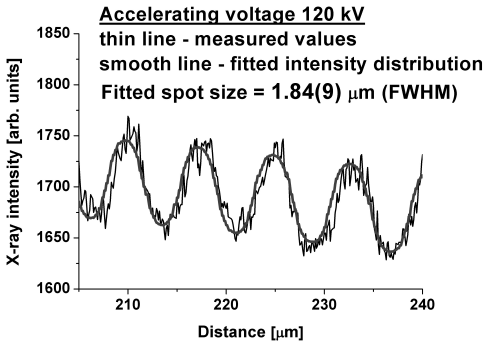

Fig. 11. Fitted value of the X-ray tube emission spot size from a projection of digitized image of the calibration tile

X rays of the tube are emitted from a spot in the target, where the electron beam is focused (Fig. 4). The size of the spot depends on the focusing current pre-defined for each accelerating voltage of the tube – however, with a possibility to manual adjustment of the current. Emission spot size as a function of the focusing current at the 100 kV tension is shown in Fig. 12. Each data point is an average value of several measurements.

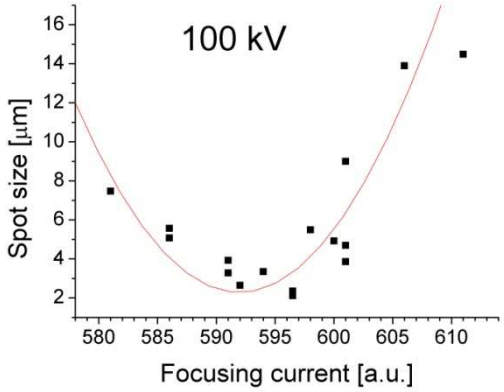

Fig. 12. Resolution of the X-ray tube versus *focusing current. Acceleration voltage is equal to 100 kV*

Resolution of the tube measured for the optimized value of the focusing current was equal to about 2 μm at 100 kV and was deteriorating to about 4 μm for low accelerating voltage (Fig. 13).

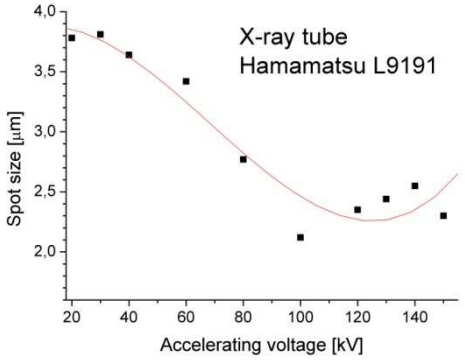

Fig. 13. X-ray tube resolution as a function of accelerating voltage

The X-ray tube flux has been measured with a use of Amptek XR-100CR (Si-pin) and XR-100T-CdTe (CdTe diode) detectors. An example of the X-ray spectrum obtained with the Ti target is shown in Fig. 14. Continuous part of the spectrum is the bremsstrahlung radiation mainly from Be window material while the sharp lines are characteristic lines from excitations of the target material, in this case Ti. Intensity of the radiation for a given target depends on the target current and accelerating voltage of the tube. Figures 15 and 16 present correspondingly intensity of the characteristic line (4.5 keV) and of the continuous part of the

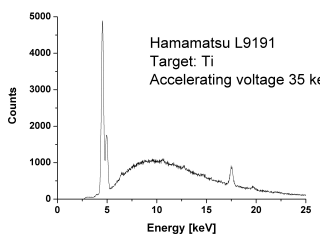

Fig. 14. X-ray spectrum for the Ti target. Higher energy peaks are Mo lines from the tube construction material.

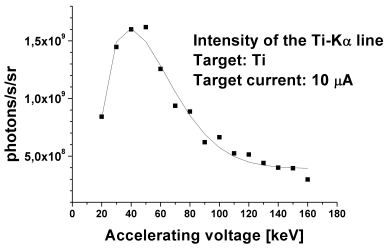

Fig. 15. Intensity of the Ti-K_α line as a function of accelerating voltage

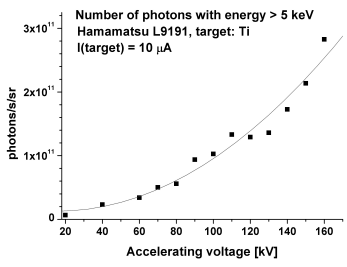

Fig. 16. Intensity of the bremsstrahlung radiation versus X-ray tube voltage

spectrum as a function of accelerating voltage measured for the Ti target at the maximum target current of 10 µA (tube current equals to about 200 µA).

2.4. Examples of tomography images and discussion of artefacts

In order to evaluate the performance of the system as well as the performance of the reconstruction process several tomography experiments were carried out with centimeter and millimeter size objects. Fig. 17 presents reconstructed tomography images of a transistor and its photo. In reconstructed images, a thin wire inside the transistor is clearly visible. Images were reconstructed from 400 projections each of 500 x 333 pixels. Projections were obtained with a use of the polyenergetic cone beam emitted from the X-ray tube equipped with the W target. Acquisition time of a single projection was 20s. The reconstruction process was accomplished with a use of filtered back projection algorithm implemented in the Octopus package [8]. The reconstructed image consists of 500 x 500 x 311 voxels, 10 x 10 x 15 μm^3 size each one.

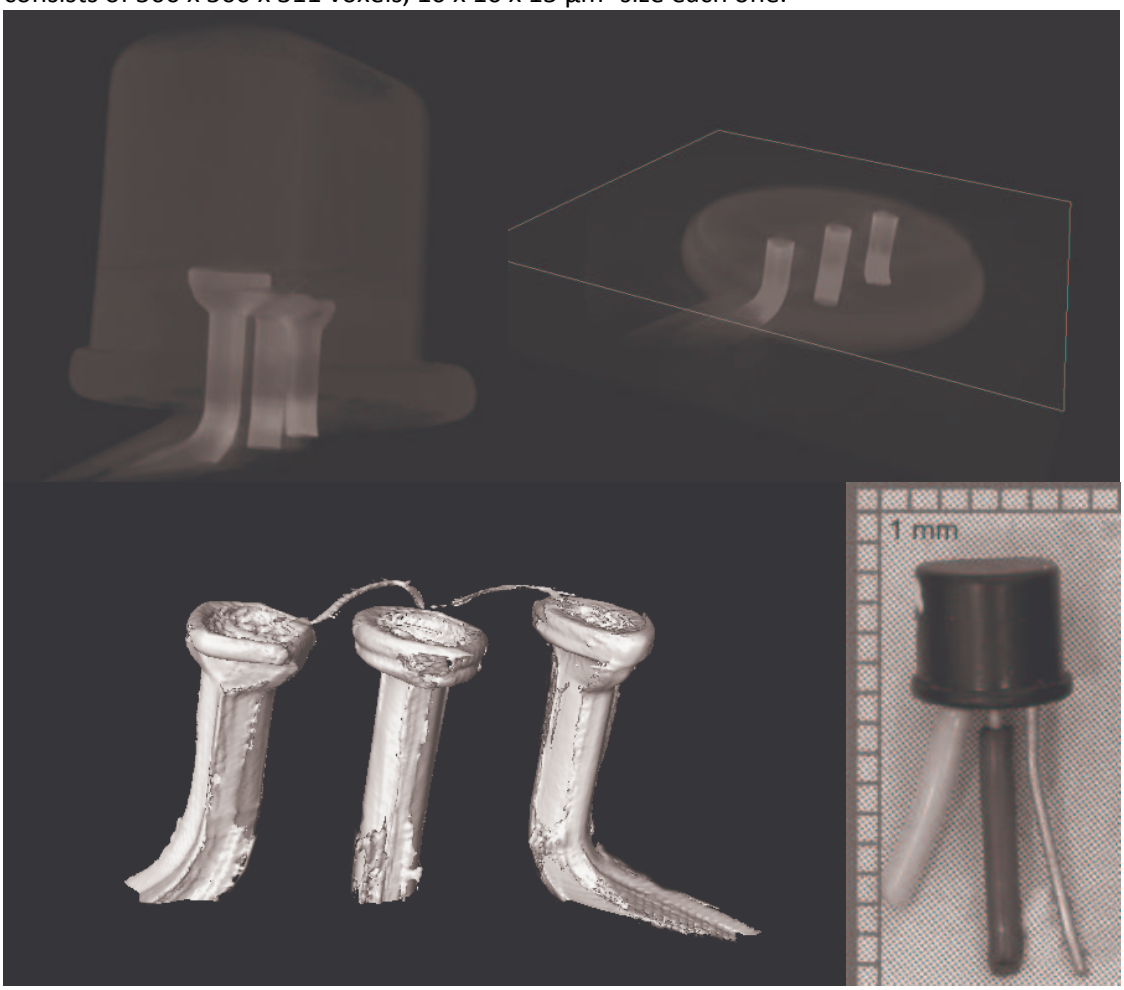

Fig. 17. Tomographic images of a transistor. Bottom right side of the figure presents a photo of the object.

In order to check the possibility of imaging geological samples a few tests were carried out. Fig. 18 shows tomography images of a sample of andesite rock and its photo. Reconstruction was obtained from 500 projections (744 x 666 pixels), acquired with a use of the W target. Integration time of single projection was about 30 s. Tomography images contain 744 x 744 x 500 voxels. Single voxel size is equal to about 10 x 10 x 10 μm^3.

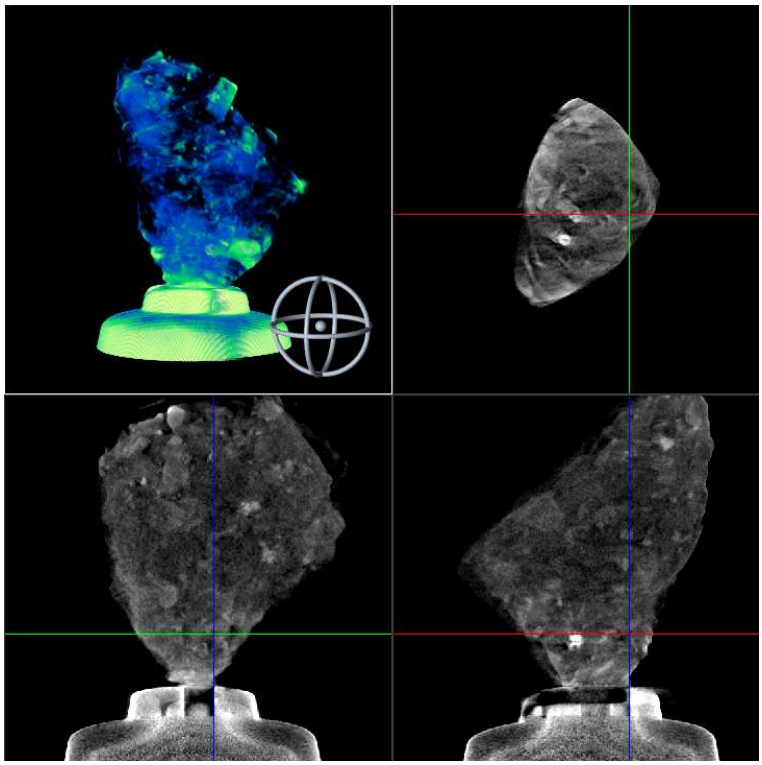

Fig. 18. Tomography images of a sample of andesite rock.

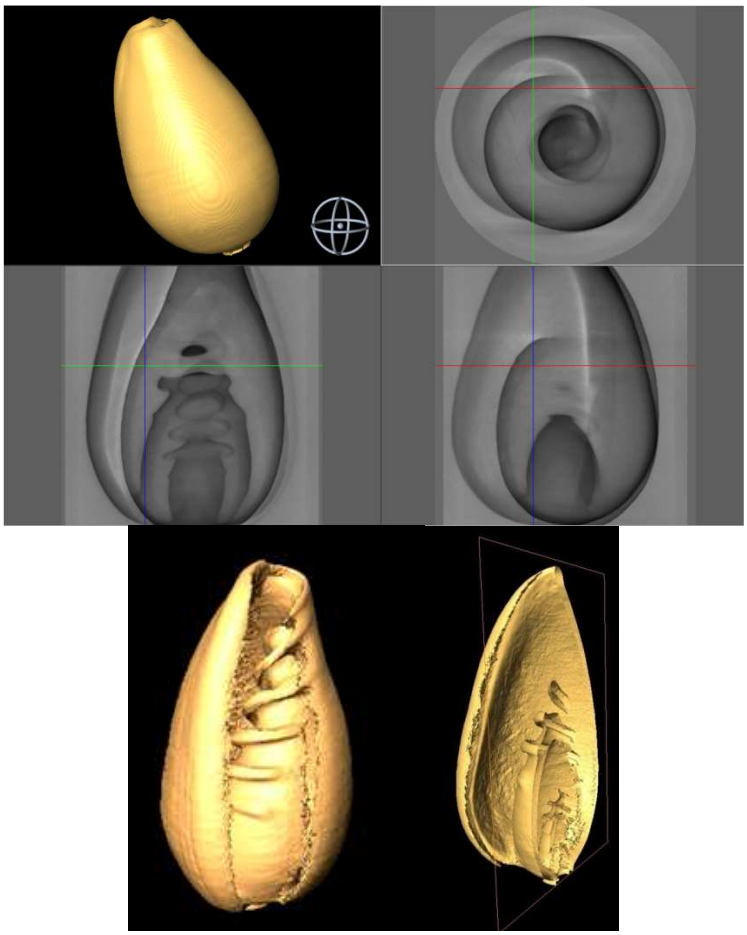

Fig. 19. Tomography images of a shell. The image contains 437 x 437 x 600 voxels reconstructed from 500 projections (744 x 666 pixels), acquired with the use of W target.

Additionally, tomography images of about 2 centimeter long shell (Fig.19), a small bulb (Fig. 20) and other samples were obtained. The samples were chosen in order to cover wide range of specimens' density.

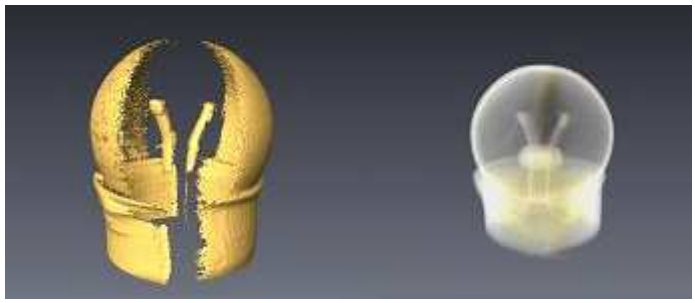

Fig. 20. Tomography image of a small bulb.

Images are reconstructed from projections, which are subjected to noise and errors. Any error of projections' measurement influences the reconstructed images. In reconstructions several types of artefacts can be observed. The first artefact type is caused by mechanical instability of the specimen during the experiment. Vibrations cause errors in projections and, in consequence, distortions in the reconstructed slices. To avoid this artefact it is necessary to use the exposition time as short as possible. Also, the overscan technique, providing data redundancy and averaging inconsistencies in the projection dataset, was used in order to minimize motion artefacts. The second type of artefacts is related to so call "rings". They appear as an increase or decrease in the image intensity values along a circle (or part of a circle), centered at the centre of rotation of the system. The artefact is caused by different sensitivity of some pixels in the CCD matrix.

First method used by us to reduce the ring artefacts is a "flat field correction". This is a simple method of error correction that is accomplished by taking the image of the beam without the measured sample before and after projection acquisition. The data are next used to sample image normalization. This method can correct to some degree errors caused by inhomogeneous sensitivity of pixels in the CCD camera as well as local inhomogeneities in the X-ray beam intensity. Besides flat field images correction, the so called "dark images" were also collected, in order to correct dark current of the detector. Dark images are subtracted from the projection images and the open beam images. However, the above approach cannot remove ring artefacts entirely. So the next step is the post-processing of tomography images. This process is accomplished with a use of the algorithm of sinogram processing during the reconstruction implemented in the Octopus package (sinogram is a consecutive sequence of sample image projections).

Ring artefacts are recognized in the sinograms as vertical lines from top to bottom. Reduction of these artefacts is made in the following way: for each sinogram the average of each column is calculated and compared to the average value of the nearest neighbor columns. When deviating by more than a chosen level, the pixel values in the column are multiplied by a correction factor so that the average of the column becomes equal to the median of the averages of its neighbors. This procedure performs better than the commonly used method of applying a low pass filter in the perpendicular direction which introduces unnecessary blurring [11]. Fig. 21 presents reconstructed slice with, and without ring filtering.

A use of polyenergetic radiation can cause an appearance of the "beam hardening" distortions. As the polyenergetic beam of X-rays passes through an object, the mean energy of the beam increases, because the lower energy photons are more absorbed than the higher energy ones. This effect can also lead to artefacts (see [12]). The most noticeable effect is the cupping of reconstructed samples. A reconstructed density value in the centre of the sample is seemingly lower than at the sample edges (Fig. 22). The simplest way to reduce the beam hardening artefacts is to use the "pre-hardening" filter absorbing low energy part of the X-ray beam, such as 0.5 mm thin filter made from aluminum or copper. Unfortunately, this method causes a reduction of the X-ray beam flux. Complementary to the filter method is a use of the beam hardening correction algorithms

implemented in the Octopus package. This software offers two correction methods for a two phase object (like material + air): an advanced beam hardening correction algorithm and a faster polynomial correction [13].

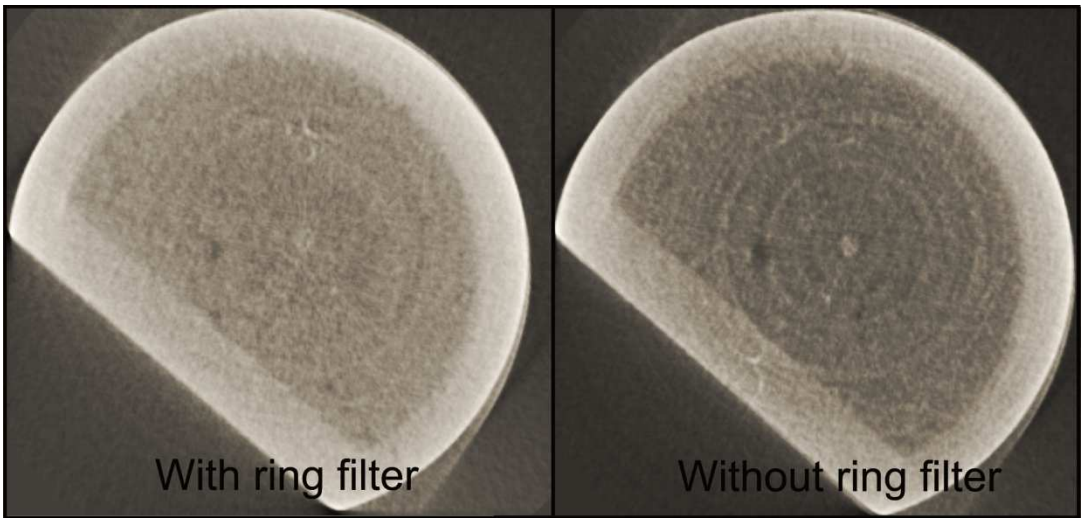

Fig. 21. Example of reconstructed slice images with and without the ring filtering.

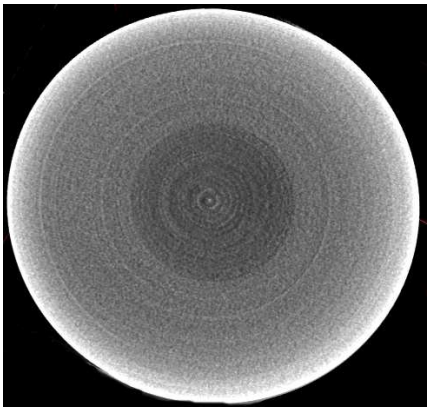

Fig. 22. Appearance of the beam hardening artefact in the image of reconstructed slice.

3. DESCRIPTION OF THE STAND FOR TARGETED IRRADIATIONS WITH X-RAYS

3.1 Construction of the stand for irradiations

In recent years a large progress has been achieved by a common effort of numerous laboratories studying response of individual cells for targeted ion beams, permitting to control precisely a dose delivered to the cell and its localization within the cell. However, only a few X-ray microprobes are used in such studies [15, 16]. In the experiments biological consequences of radiation damage, mostly of DNA damage by targeted or non-targeted ionizing radiation is studied. While physics of radiation damage induced by ion or X-ray irradiation is similar (direct ionization or excitation, ionization by secondary electrons, and chemical reactions with free radicals or reactive oxygen species generated by the radiation), biological effects differ significantly depending on the type of radiation. Single strand breaks of DNA (SSB) usually are quickly repaired by the cell, while double strand breaks (DSB) need longer time to repair and often cannot be repaired, leading to apoptosis or to genomic instability. A number of DSB events created by the bombarding ion or photon depend on the density of ionization events, therefore on the LET (linear energy transfer) value of the radiation,

very different for ions and for X-rays. Therefore, investigations performed with a use of nuclear microprobes should be accompanied with similar experiments performed at the X-ray microbeams. Such studies are carried out at the synchrotron radiation lines, but it is cheaper to use for the experiments a dedicated X-ray microprobe basing on a microfocusing X-ray tube. Microprobes of this type are constructed and used at the Gray Laboratory [15, 16], and the microprobe constructed at our institute will be used also for this task.

Experimental line for targeted irradiations of mammalian cells consists of a microfocusing X-ray tube, an optical system re-focusing X-ray beam outside the tube, a high precision stand for positioning individual cells at the focus of X-ray beam, and an optical microscope to control the position of cells. During aligning and testing procedures an X-ray CCD camera was used, taken from the experimental line dedicated for the CMT experiments. The microprobe is located inside a 2 mm thick lead box with a movable front window made of 1 cm thick lead glass for radiation protection of the experimentalists. The X-ray tube and CCD camera are described in the text above. As the optical microscope controlling positioning of cells a zooming long distance microscope Thales Optem Zoom-160 [17] was chosen. Construction of the stand for positioning irradiated cells is based on high precision micro-translation stages M-111 produced by Physik Instrumente GmbH [18] with minimum incremental motion of 0.05 μm and repeatability of 0.1 μm.

Targeted irradiations of cells require a beam refocused outside the X-ray tube. For radiobiology experiments the X radiation energy of 4.5 keV (Ti-K_α line) was chosen. X-rays of this energy can be focused either with zone plates or with reflecting mirrors. Zone plates are cheaper and the aligning procedure with zone plates is simpler, however the plates are easily breakable and are quickly destroyed by the radiation, while mirrors (when working in vacuum or in He atmosphere) have nearly infinite life. Also, it is expected that a larger intensity of the focused beam can be achieved with a comparable source-to-focus distance. Therefore, it was decided to focus the beam with elliptical multilayer mirrors manufactured at the Rigaku Innovative Technologies [19]. Remotely operated mirrors in the Kirkpatrick-Baez geometry (Fig. 28), designed for the present microprobe are shown in Fig.23. Their source-to-focus distance is only 30 mm and the solid angle of the optical system is about

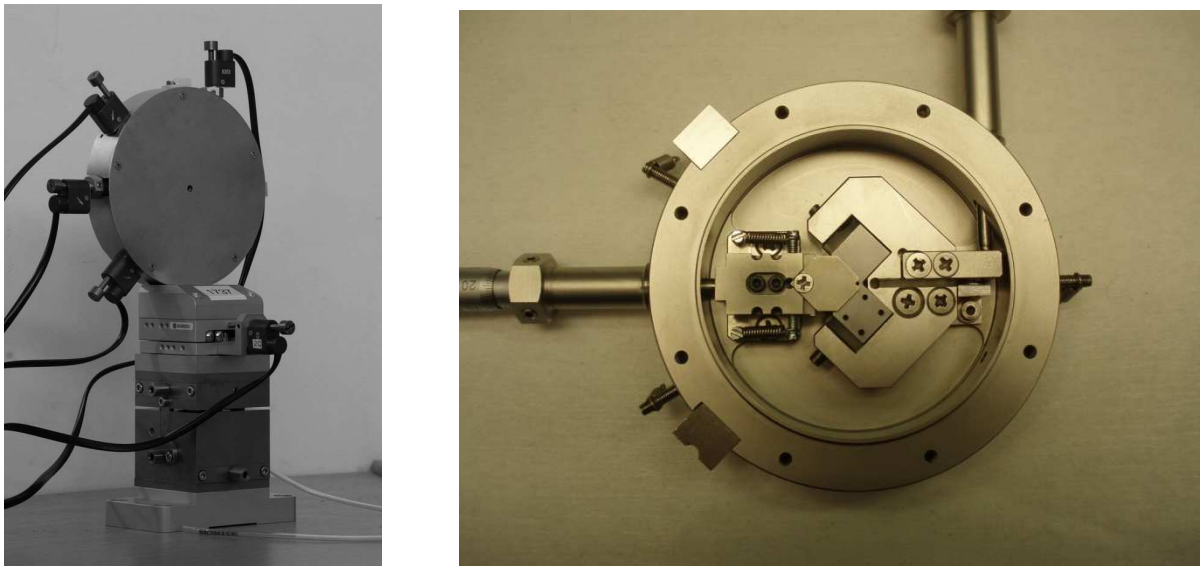

Fig. 23. Multilayer elliptical mirrors focusing system. Left picture: external view with shown five piezoelectric motors controlling the Bragg angles and perpendicularity of mirrors as well as the source-to-mirrors distance and solid angle of the optical system. Right: inside view of the mirrors chamber.

1.5e-4 sr. Mirrors are working in a vacuum and He tight chamber with thin Be windows. The magnification ratio is equal to 1, and the expected size of the focus is about the same as the size of emitting spot in the tube. By using the multilayer coating of reflecting surfaces the mirrors are working also as a monochromator what greatly simplifies interpretation of the experiments.

3.2 Alignment and testing procedures of the focusing system

X-ray focusing mirrors usually are working in pairs arranged in the Kirkpatrick-Baez geometry, each mirror is perpendicular to the other and focusing only in one plane. Beam reflected from both mirrors is focused to a point-like spot. High reflectivity of the mirror surface is achieved either under total reflection principle by using grazing angle of incidence, or by reflection at the Bragg angle from a multilayer surface. Mirrors delivered by the Rigaku Innovative Technologies are elliptical mirrors with multilayer Cr/C surface with d=3.1 nm period. Theoretical rocking curve and the reflectivity versus photon energy curve for the mirror surfaces calculated using formulae given in [20] are presented in Fig. 24a and 24b, respectively. As seen in Fig. 24b, the mirrors can be used as a monochromator reflecting only the Ti-K_α line and absorbing the K_β line.

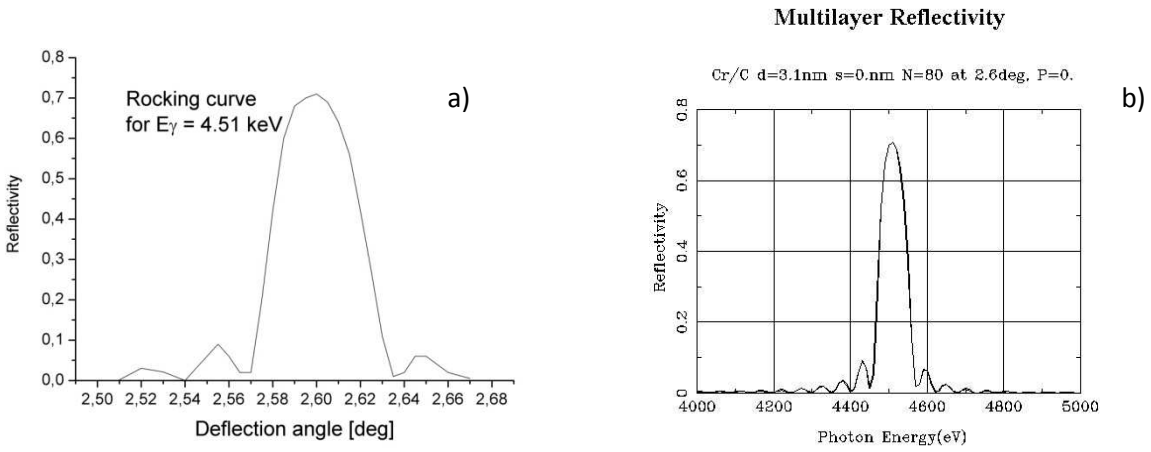

Fig. 24. Rocking curve (a) and reflectivity (b) calculated for the Rigaku multilayer mirrors surface

Chamber of the focusing mirrors is equipped with five remotely operated piezo-motors enabling a change of the incidence angle of each mirror, their perpendicularity, distance of the focusing system from the front window of X-ray tube and changing position of a screen defining acceptance angle of the focusing system. Two other movements, i.e. the height of the mirror system and its position perpendicular to the optical axis are adjusted manually. Image of X-ray beam passing through the focusing system after its alignment, and registered in the CCD camera placed at a distance a few cm behind the focal plane is shown in Fig. 25. At two sides of a large square spot from direct, not reflected beam are seen two narrow bars of the beam reflected at the Bragg angle from a single mirror and a point-like spot of the beam reflected from both mirror surfaces. Energy spectra measured for the direct and for focused beam are shown in Fig. 26a and 26b, respectively.

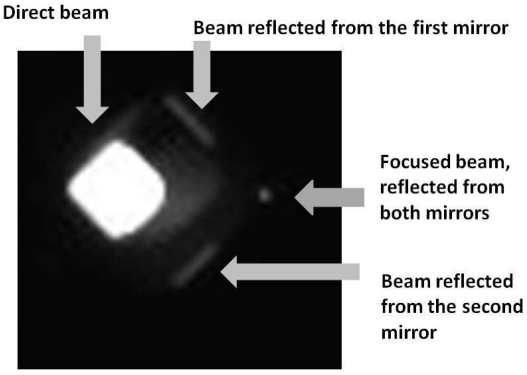

Fig. 25. Beam image registered at 3 cm from the focal plane

A size, shape, and spatial position of the focused beam are determined by probing it with a movable sharp knife edge and monitoring image of the beam with the CCD camera. According to the technical description,

one focal point of the elliptic shape of the mirror is located 3 mm from the window of chamber for mirrors. If the source of radiation is located in this focal point, its image will be found at a distance of

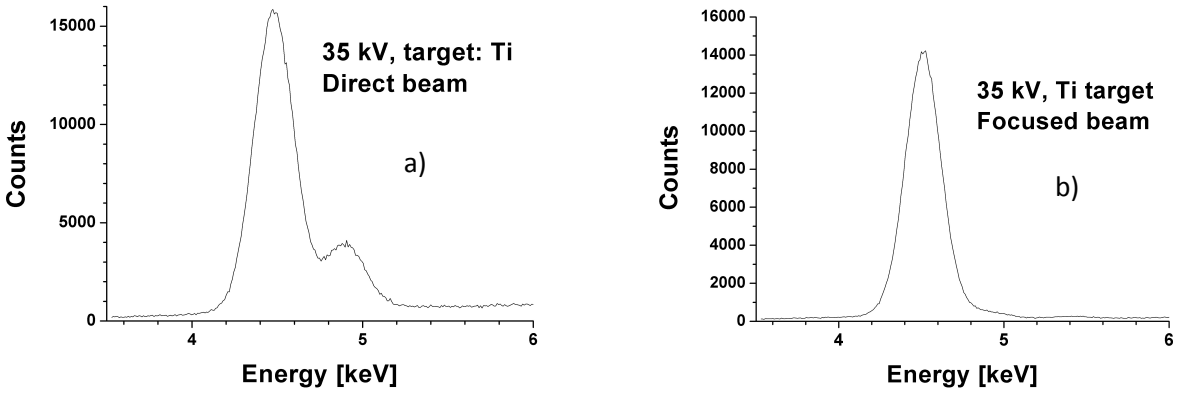

Fig. 26. Energy spectra of the direct X-ray beam (a) and beam focused with Rigaku mirrors (b)

30 mm from it, in a focus at the other side of the chamber. To prove that a series of measurements were performed for different values "***a***" of a distance of the mirrors chamber from the emission spot in the tube and registering a size of the beam as a function of "***x***", a distance from the other side of the chamber. The results are shown in Fig. 27. From analysis of the results one can deduce that a

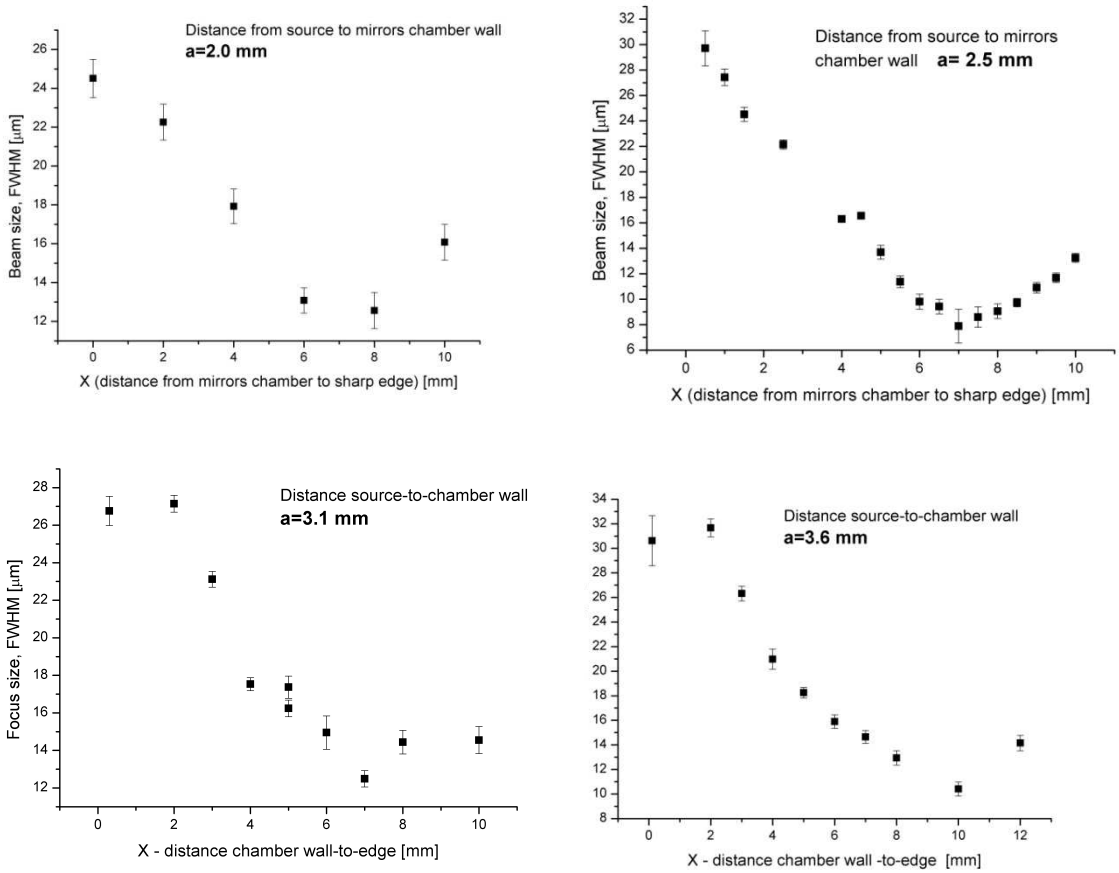

*Fig. 27. Search for the focal plane: beam size dependence on a distance "**x**" from the mirrors chamber taken for different values of source-to-chamber distance "**a**"*

distance of the first focal point is indeed at 3 mm from the chamber, but a distance between foci of

ellipse is equal to 31 mm, one mm more than specified. The measurements were performed at low accelerating voltage of the X-ray tube, with emitting spot size of about 3.5 µm.

The expected size of focus should be comparable to the size of source. However, the smallest value of focus size achieved so far was about 7 µm, what means that the optical axis of focusing system still does not match perfectly X-ray beam direction. Aberrations of the optical system cannot change so much the size of focus.

Intensity of the focused beam depends on the solid angle of the optical system what can be changed by screening with a movable plate the beam reflected from the mirrors. At maximum opening of the mirrors the measured intensity of the focused beam is about 4200 photons per second, what gives the delivered energy rate of 19 MeV/s. Taking into account that about 3% of this energy is deposited in a layer of biological material of a thickness of 5 µm (an average thickness of the cell nucleus), we expect that the delivered dose rate to the cell nucleus will be about 0.7 Gy/s.

4. DESCRIPTION OF THE STAND FOR µXRF AND TXRF EXPERIMENTS

4.1 Components of experimental facility

Measurements performed with the micro-fluorescence induced by X-rays method (µXRF) deliver information on the concentration of elements in the investigated sample. With this method one can reach very high sensitivity in determination of 2-D maps of trace elements concentration with the spatial resolution determined by the size of the focused X-ray beam spot. Even higher sensitivity can be reached in experiments of the total reflection XRF (TXRF) when the X-ray beam illuminates the sample under a grazing angle, smaller than the critical angle of total reflection. In such experiment the main beam is totally reflected from the sample surface and does not reach the detector which is placed usually at 90^{o} to the beam direction and registers only the radiation induced from the sample without any background from the main beam. Very high sensitivity is achieved at a cost of that a good spatial resolution is possible only in one direction.

The facility for µXRF and TXRF experiments is composed of the X-ray tube, a focusing mirrors system, a stand for positioning the sample in a focus of mirrors, and the X-ray detector. Position of the sample is achieved by remotely controlled linear and rotation actuators made by Standa [1]. X-rays emitted from the sample are registered in an 80 mm^2 Si(Li) detector of a model LS80155-DS produced by the Princeton Gamma Tech Instruments Inc. [21]. The detector resolution is 155 eV for the 5.9 keV line. Data acquisition system is based on the electronic modules manufactured by the XIA LLC [22].

X-ray focusing system of the facility is composed of two elliptical mirrors arranged in the Kirkpatrick-Baez geometry (Fig. 28). The mirrors, shown in Fig. 29, are manufactured by the Xradia Inc. [9]. While the Rigaku mirrors used in the stand for targeted irradiations are coated with Cr/C multilayer acting as a diffraction grid and reflecting only 4.5 keV radiation, the Xradia mirrors are coated only with a single layer of Pt with the Cr binder and are based on the total reflection principle.

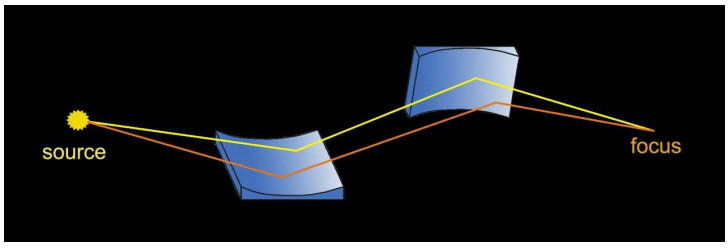

Fig. 28. Kirkpatrick-Baez geometry of reflecting mirrors

Therefore, they are not energy selective, reflecting radiation of all energies with incidence smaller than the critical angle, i.e. in the energy range of 4-23 keV. Usually the mirrors will be used for focusing the characteristic lines of Mo-K_α (17.5 keV) or Ag-K_α (22.2 keV). The mirrors are made of

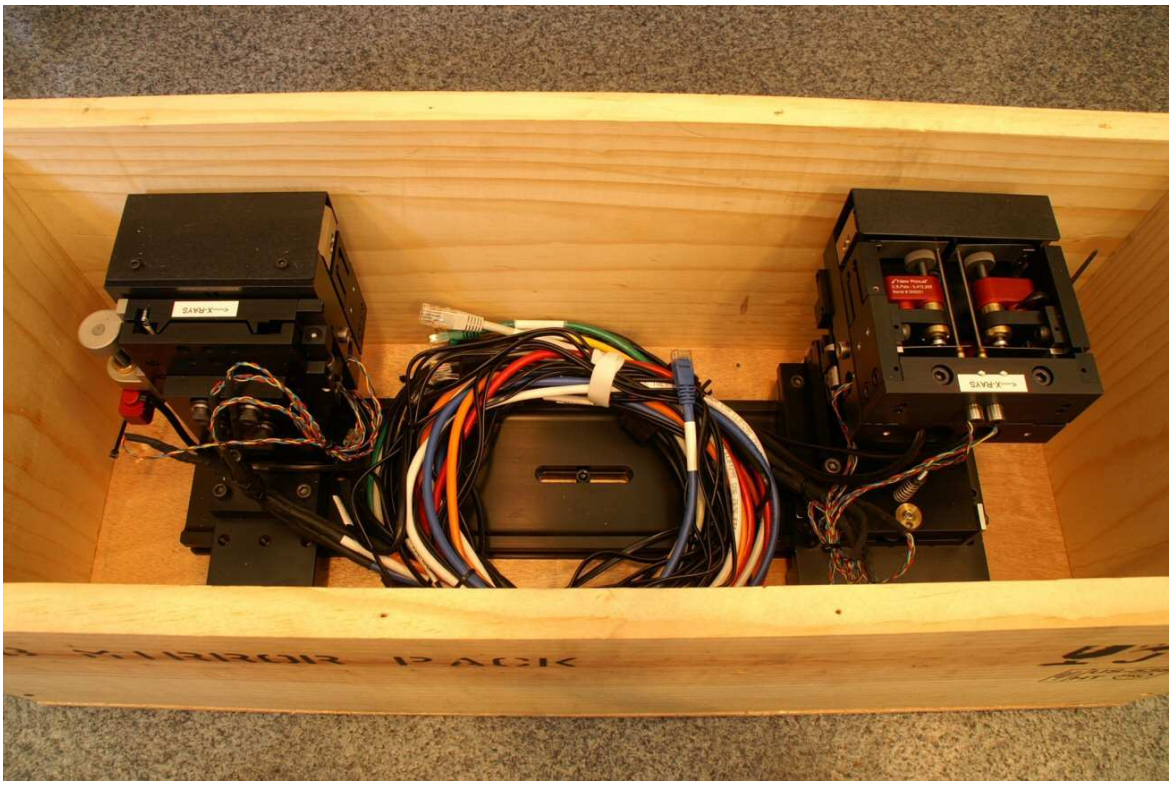

Fig. 29. Total reflection mirrors system manufactured by Xradia Inc.

flat silicon plates coated with Pt and bent to elliptical shape with remotely controlled piezoelectric motors. The source-to-focus distance is equal to 440 mm and the collection solid angle of the system is equal to about 8 x 10^{-6} sr. The focusing distance can be slightly changed by the controlling motors. In the same stand also parabolic mirrors can be used, delivering the parallel X-ray beam and the microprobe is equipped also with such mirrors for its future use in the crystallography experiments.

4.2 Testing electronic modules for X ray detection

The developed system of the data acquisition of the microprobe is a (relatively) low cost / fast development solution based on the signal processor manufactured by XIA LLC [22]. The heart of the system is the DXP–XMAP unit designed as the PXI (Extended CompactPCI) module. System replaced the traditional, analog solution built around the NIM / CAMAC electronics that has been in use at the IFJ ion microprobe during last ten years. Detector signals (up to four tracks in current setup) are digitized directly at the preamplifier outputs, thus reducing the use of traditional nuclear electronics modules virtually only to detector and preamplifier power supplies.

All subsequent signal processing, including event timing, pulse filtering, pile–up inspection, thresholding, dead time correction, etc. is performed in the DSP memory using powerful data processing algorithms. Data are collected / transferred from the PXI crate to the supervising microcomputer in a double buffer fashion (Fig. 30), while the microprobe control (detection synchronization, pixel advancing, beam blanking, etc.) may be realized using traditional electronics

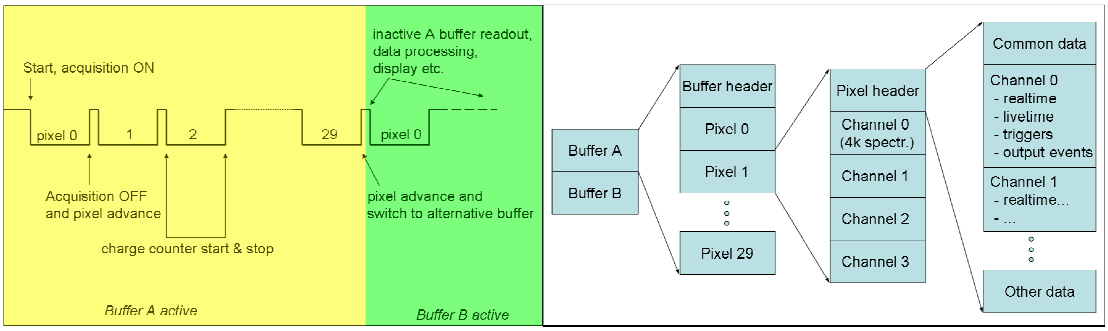

Fig. 30. Data collected/transferred from the PXI crate to the supervising microcomputer in a double buffer fashion

either by hardware (gated) signals or through direct software calls. The extensive driver libraries with high level function calls allow smooth implementation of the DSP hardware into existing data collection system.

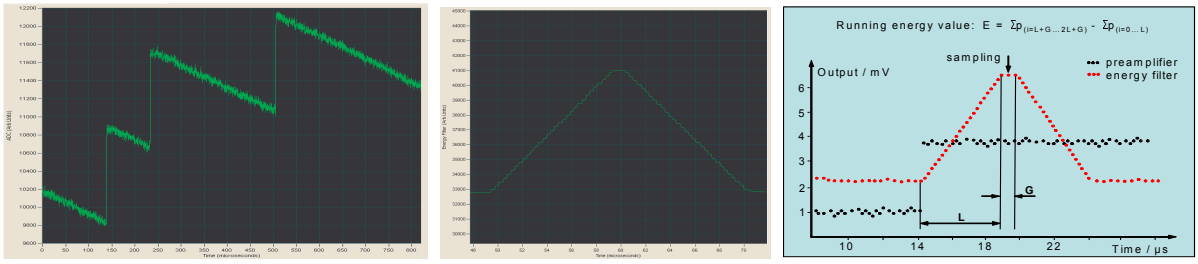

Fig. 31. X-ray signals at the ADC input, the pulse after energy filter, and the idea of trapezoidal filtering of the sampled preamplifier output. Peaking time L corresponds to about ½ of the time shaping constant of the analog system.

The advantage of the system over traditional, analog solution is huge and includes not only the tremendous simplification of the data acquisition system. The digital system is characterized by the excellent performance even at high input rates without any additional electronics, cf. Fig. 32 below.

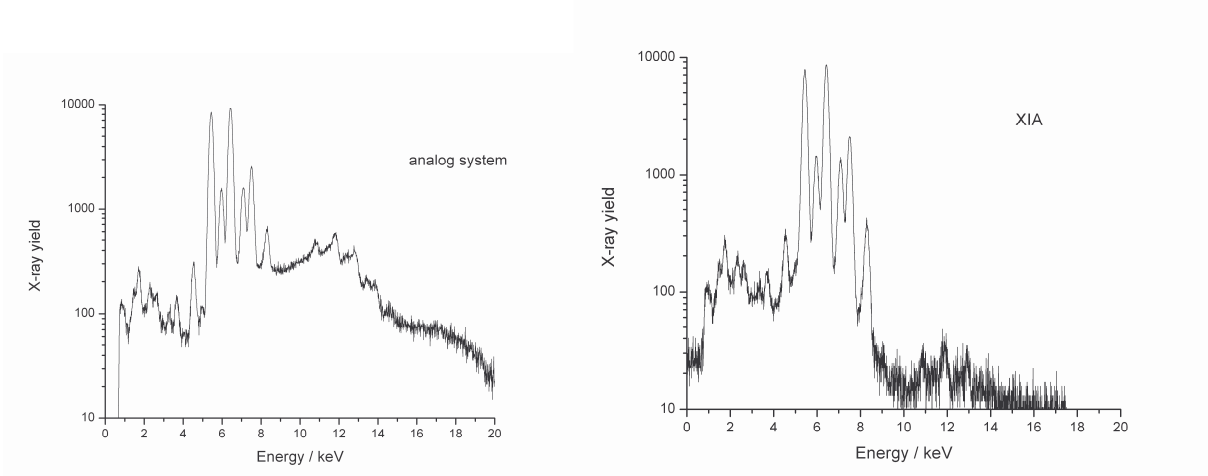

Fig. 32. Comparison of spectra acquired with the old, analog spectroscopy system of the Krakow microprobe (left figure, no pile-up rejector) and the new DSP version (right). X-ray input rate was about 30k cps. Time shaping constant of analog system was 6 µs, while peaking time L of the new system was 10 µs. Please note the superior XIA resolution.

Another advantage is easy software modification of the signal processing parameters allowing tailoring the system performance to varying experimental conditions, see below:

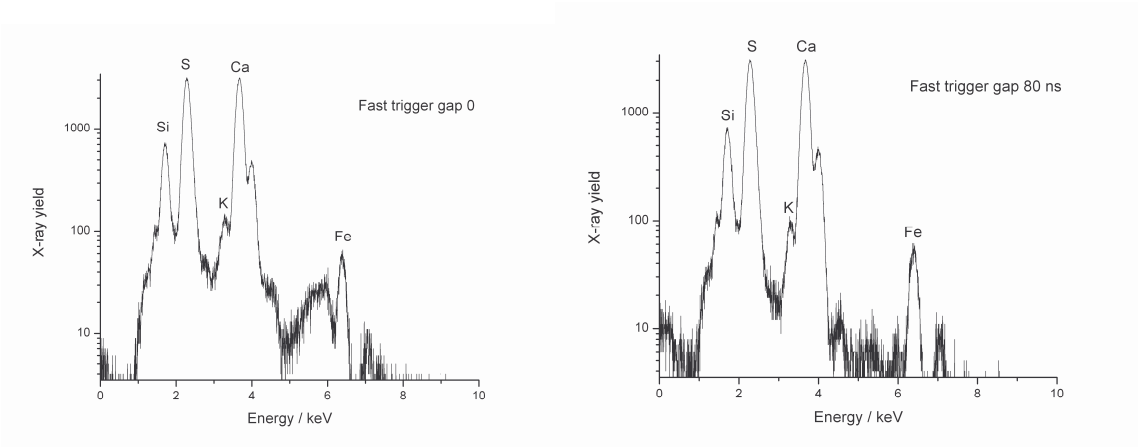

Fig. 33. Comparison of spectra taken with default fast trigger settings and with increased fast trigger gap. Input rate was 10k cps.

CONCLUSIONS

A multipurpose, high resolution X-ray microprobe has been constructed and the component elements of the microprobe have been tested. From numerous possible applications of the microprobe the method of computed microtomography (CMT) has been introduced into routine use. In future, also phase-sensitive CMT method will be introduced. A stand for targeted X-ray irradiations is presently in the final phase of testing. Alignment of the focusing mirrors still requires a better adjustment. Other applications of the microprobe will be tested in the nearest future.

ACKNOWLEDGEMENTS

Purchase of hardware and software for the X-ray microprobe was supported by the Foundation for Polish Science and Technology, grant No. 222/FNiTP/119/2005. Partial support from the MP0601 project of COST is also gratefully acknowledged.

REFERENCES

[1] *http://standa.lt*

[2] *http://jp.hamamatsu.com/resources/products/etd/pdf/MFX_TLSO1063E03.pdf*

[3] *http://www.attocube.com/nanoPOSITIONING/nanopositioning.htm*

[4] *http://www.photonic-science.co.uk*

[5] *http://www.mediacy.com*

[6] *http://www.xraylab.com*

[7] *http://3dviz.mc.com/products/avizo.asp*

[8] M. Dierick, B. Masschaele, L. Van Hoorebeke, "Octopus, a fast and user-friendly tomographic reconstruction package developed in LabView (R)", *Measurement Science & Technology* **15(7)** (2004) 1366-1370.

[9] *http://xradia.com/Products/targets.html*

[10] S. Bożek, J. Bielecki, J. Baszak, H. Doruch, R. Hajduk, J. Lekki, Z. Stachura, W.M. Kwiatek, "X-ray microprobe – a new facility for cell irradiations in Krakow", accepted in *Nucl. Instr. Methods B (2009)*.

[11] Manuel Dierick, "Tomographic Imaging Techniques using Cold and Thermal Neutron Beams", PhD thesis, Gent University 2005.

[12] Julia F. Barrett, and Nicholas Keat, "Artifacts in CT: Recognition and Avoidance", *RadioGraphics* **24** (2004) 1679-1691.

[13] J. Vlassenbroeck, M. Dierick, B. Masschaele, V. Cnudde, L. Van Hoorebeke, P. Jacobs, "Software tools for quantification of X-ray microtomography at the UGCT", *Nucl. Instrum. Meth. A* **580** (2007) 442–445

[14] J. Bielecki , S. Bożek, J. Lekki, Z. Stachura, W. M. Kwiatek, „Application of the Cracow X-ray microprobe in tomography", accepted in *Acta Phys. Polon. A* (2009).

[15] M. Folkard, B. Vojnovic, G. Schettino, M. Forsberg, G. Bowey, K.M. Prise, B.D. Michael, A.G. Michette, S.J. Pfauntsch, "Two approaches for irradiating cells individually: a charged-particle microbeam and a soft X-ray microprobe", *Nucl. Instrum. Meth. B* **130** (1997) 270-274

[16] M. Folkard, G. Schettino, B. Vojnovic, S. Gilchrist, A.G. Michette, S.J. Pfauntsch, K.M. Prise, B.D. Michael, "A Focused Ultrasoft X-Ray Microbeam for Targeting Cells Individually with Submicrometer Accuracy", *Radiat. Res*. **156** (2001) 796-804

[17] *http://www.thales-optem.com*

[18] *http://www.physikinstrumente.com*

[19] *http://www.rigaku.com*

[20] B.L. Henke, E.M. Gullikson, J.C. Davis, *At. Data and Nucl. Data Tables* **54** (1993) 181 and *http://henke.lbl.gov/optical_constants/*

[21] *http://www.pgt.com*

[22] *http://www.xia.com*

[23] J. Lekki, J. Bielecki, S. Bożek, Z. Stachura, W.M. Kwiatek, „Design of the Kraków X-ray microprobe facility for targeted X-ray irradiations of biological objects", accepted in *Radiation Research,* extended abstracts volume (2009)